Géotechnique **00**, 1–14 [http://dx.doi.org/10.1680/jgeot.18.P.044]

On the efficiency of slit-check dams in retaining granular flows

M. MARCHELLI*, A. LEONARDI*, M. PIRULLI*, C. SCAVIA*

Retention barriers are a common countermeasure for mitigating hazard associated with debris flows. With the aim to regulate sediment transport and retain large boulders with high destructive potential, openings are nowadays embedded in the barrier body. The rational design of size and spacing of these outlets is a non-trivial, and still open, issue. Nevertheless, its solution is necessary in order to control the clogging process and consequently guarantee effectiveness and efficiency of the barrier. In this paper, an enhanced numerical model, based on the Discrete Element Method (DEM), is presented, validated, and proposed to analyze the interaction between dry granular flows and barriers with a single outlet (slit-check dams). We identify the lower and upper value of the outlet size that cause clogging of the outlet. These are found to be a function of the channel inclination and of the frictional properties of the grains. A range of outlet sizes exists which promotes a slow and progressive clogging. The conditions that are necessary for this condition to occur are determined. This allows the barrier to perform an energy-breaking function for a longer time and require less maintenance after the event.

KEYWORDS: Debris flows, Slit-check dams, Flow/Barrier interaction, Numerical modeling, Discrete Element Method

NOTATION

r	particle radius [m]
D	particle diameter [m]
m	particle mass [kg]
I	particle moment of inertia [kg]
k_n	normal stiffness [N/m]
k_t	tangential stiffness [N/m]
α_n	normal damping coefficient [-]
α_t	tangential damping coefficient [-]
c	restitution coefficient [-]
ω	particle rotational velocity [1/s]
v	particle translational velocity [m/s]
M_r	rolling torque [Nm]
e	rolling eccentricity [m]
μ_r	rolling coefficient [-]
μ_s	friction coefficient [-]
q, p	deviatoric, isotropic stress [Pa]
ϵ_z	axial strain [-]
ϕ	angle of repose [°]
ψ	angle of internal friction [°]
S	barrier outlet width [m]
H	barrier height [m]
θ	slope inclination [°]
g	gravity [m/s^2]
v_f	flow front speed [m/s]
h_f	flow front height [m]
K	flow kinetic energy [J]
t_0	time at first impact [s]
t_stop	clogging time [s]
E_K	barrier energy-breaking efficiency [-]
E_m	barrier retention efficiency [-]

Manuscript received...
*Politecnico di Torino, Corso Duca degli Abruzzi, 24 - 10129 Torino, Italy, maddalena.marchelli@polito.it - alessandro.leonardi.ing@gmail.com - marina.pirulli@polito.it

INTRODUCTION

Debris flows are landslides of the flow type (Hungr *et al.*, 2001) and are one of the most common and dangerous hazards in mountainous regions. The effects of the flow impact against infrastructures and inhabited environments can be dramatic, due to the unpredictability, high velocity (up to 20 m/s) and destructive power that typically characterize the flowing mass (Hungr & Jakob, 2005).

In recent years, an increasing number of studies has focused on the design of structural mitigation measures able to reduce hazard and prevent damages, such as retention barriers (see Fig. 1). However, the complex composition of the flow, and the multitude of relevant scales involved, still limit rational studies to simplified models. In particular, the impact of a granular flow on a solid vertical wall has been widely studied both numerically (e.g. Albaba *et al.*, 2015; Calvetti *et al.*, 2015, 2017; Gabrieli & Ceccato, 2016) and experimentally (e.g. Canelli *et al.*, 2012; Koo *et al.*, 2017). While this benchmark remains pivotal for our understanding of the basic mechanism of stoppage and deposit of a granular mass, this type of retention barrier is no more used on the field. A vertical wall causes stoppage of the whole flowing mass, quickly filling the basin behind. The efficiency of such walls is therefore limited, and their maintenance costs high, as the basin must be quickly emptied to restore its functionality. For this reason, most retention barriers are nowadays designed to only *partially* halt the flow. Ideally, the most hazardous portion of the mass (i.e. the largest boulders) needs to be retained.

The design of the most suitable structure is however problematic. While it is clear that any type of barrier should

Fig. 1. A debris-flow retention structure located in Pollein, Aosta Valley autonomous region, Italy.

reduce the kinetic energy of the flow, the design of the filtering action requires a much more complex approach.

Using a classical approach of hydraulic engineering, the barrier can be designed to just alter the hydraulic conditions of the flow (Armanini *et al.*, 1991; Schwindt *et al.*, 2017). In this case, the retention structure reduces the velocity of the flow, and indirectly enforces grain settling, simply by a transversal restriction of the channel section. This approach was conceived for designing structures that reduce sediment transport during alluvial events. It is however less clear whether it can be successfully applied also to debris flows, because of the high solid fraction of the debris in motion, which goes well beyond the limits of validity of the hydraulic formulas (Choi *et al.*, 2016).

In alternative, the filter control can be mechanical, i.e. the grains are stopped by exploiting their frictional properties (Piton & Recking, 2016). In this case, a section restriction causes jamming of the largest grains. The jammed grains form stable structures, i.e. contact networks able to withstand loads. Depending on the shape of these networks, they can be called arches (2D) or domes (3D). The largest grains are more likely to organize in such structures, and are then trapped behind the barrier. Similar functions can be achieved also with the use of baffles (Law *et al.*, 2016) or deflectors (Ng *et al.*, 2017).

Hydraulic control operates at a timescale given by the peak discharge, which depends on the catchment hydrologic conditions and is usually of the order of hours (Armanini *et al.*, 1991). In contrast, mechanical control is mainly a function of the supply of large sediments. This operates at a much faster timescale for debris flow, where coarser grains accumulate at the front, typically within minutes.

Also due to this complexity, no standard rules today exist for a rational design of retention structures. The comprehension of the clogging mechanism of the barrier filter, as a function of its geometry and of the flow characteristics, needs to be improved. This limits the possibility to propose and validate alternative geometrical configurations for the barrier, and to aim at a rational use of material and resources. The development of a reliable and efficient numerical method able to evaluate the effectiveness and efficiency of retention barriers is therefore necessary (e.g. Choi *et al.*, 2016; Shima *et al.*, 2016).

In this paper, a numerical model based on the Discrete Element Method (DEM) is presented, validated and proposed to analyze the interaction between dry granular flows and barriers embedding a single vertical outlet (slit-check dams). The framework is used to reproduce a granular flow inside an idealized channel, where a barrier is set. The flow mass is as a first step idealized as a collection of dry particles, therefore neglecting the presence of a fluid phase (Leonardi *et al.*, 2018). These particles represent the coarsest grains of the flow, i.e. those most likely to clog the outlet of a barrier. The model is based on a numerical code developed by Leonardi *et al.* (2014), which has been recently used to simulate the impact of a flow on a wire-net barrier (Leonardi *et al.*, 2016). In this precedent work, the mechanism is however notably different in that the barrier was set to completely halt the grains. In a slit-check dam the opening is usually much larger than the reference grain size. The relevant mechanism here, as will be discussed in detail, is the creation of granular arches that clog the outlet. In order to correctly simulate this behavior, the code has been enhanced by implementing static friction and rolling resistance in the contact model.

In the following sections, the enhanced numerical framework is first presented, and then validated by comparison with previous numerical and experimental studies. Before moving to the slit-check dam study case, the effects of the contact model on the frictional properties of the granular mass are investigated, leading to the formulation of a constitutive model for the grains. This allows to link the model parameters to measurable properties of natural granular material.

The setup of the numerical experiments is then described, and a simulation set is run in order to identify the main mechanisms of interactions between flow and barrier. For a wide range of channel inclinations and outlet sizes, the final clogging configuration and the energy-breaking efficiency are

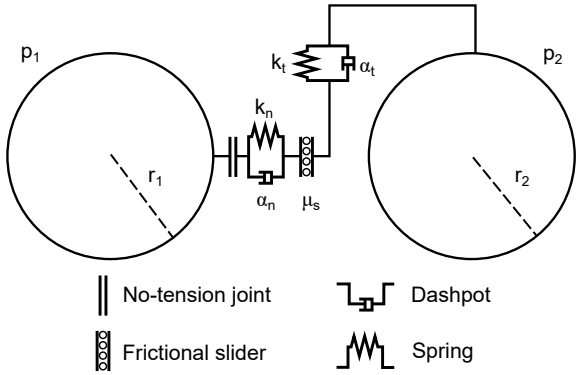

Fig. 2. Conceptual representation of the contact model.

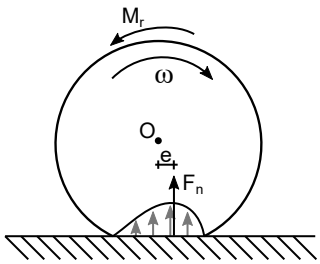

Fig. 3. Conceptual representation of the rolling-resistance model. The normal force F_n generates an extra torque due to an imposed eccentricity $e = \mu_\mathrm{r} r$.

determined. For a given slope, we are therefore able to identify the slit size that yields the most desirable behavior. A summary of the implication for the design of this type of slit dams, and an outlook on possible further developments, is given in the conclusions.

DESCRIPTION OF THE DEM NUMERICAL APPROACH

The numerical tool used for all simulations presented here is based on an enhanced version of the code described in Leonardi *et al.* (2014). The code allows for coupling with a fluid phase, but only the DEM phase has been enhanced and used at this stage. To a certain extend, the grains can be imagined as representing only the coarsest component of the granular mass. The possible implications of this choice are discussed in detail in the conclusions.

The code uses a standard DEM approach, with forces exchanged by pairs of particles whenever a contact occur. The contact model is shown in Fig. 2. Forces are computed in the normal and tangential direction by using linear springs of stiffness k_n and k_t, and damping elements of constants α_n and α_t, therefore with a constant coefficient of normal restitution c. More details about this model can be found in Leonardi *et al.* (2014). The same properties are applied to wall-particle and particle-particle contacts, unless differently specified. The contact stiffness is sufficiently high to keep the system within the rigid limit, as defined by Roux & Combe (2002). In this way, compressibility does not affect the overall kinematics of the system.

In order to allow for the creation of stable structures inside the granular mass, the tangential contact model has to be able to sustain tangential stresses also without deformations. To this aim, following a popular approach (Luding, 2008), a spring-like resistive force is initialized any time a contact occurs. The force is proportional to the relative displacement of the two points of initial contact on the surfaces of the two particles. The maximum force in the tangential direction is capped by a Coulomb-like criterion, with a constant coefficient of sliding friction μ_s.

The employed model relies on geometrically perfect spheres for representing the particles. This is generally a poor choice for simulating real granular materials. Assemblies of spherical particles are known to be less compressible than those composed of irregular grains (Iverson, 2015), thus creating more resilient arches. Furthermore, perfect spheres are not able to support stable structures on an incline. This makes their use for the target study of a granular flow impinging on an open barrier problematic. A possible solution would be to use non-spherical particles, such as those obtained by aggregating a set of spheres (Leonardi *et al.*, 2014). An alternative, employed by Teufelsbauer *et al.* (2009), is to reduce the rotational velocity of the spheres rolling on an incline, proportionally to the number of sustained contacts. A third solution, more computationally-efficient, is the addition of rolling resistance to the contact model (Girolami *et al.*, 2012). We follow this last approach, and assign to the force in the normal direction an eccentricity e, see Fig. 3. A torque is therefore generated, always opposing rotational motion:

$$M_\mathrm{r} = \mu_\mathrm{r} F_\mathrm{n} \frac{\omega_\mathrm{rel}}{|\omega_\mathrm{rel}|} \tilde{r} \tag{1}$$

where $\mu_\mathrm{r} = e/\tilde{r}$ is the coefficient of rolling friction, with $\tilde{r}$ an effective radius $\tilde{r} = r_1 r_2/(r_1 + r_2)$. With this addition, the granular assembly can create stable heaps on a flat surface. This rolling model is conceptually very similar to the one described by Zhou *et al.* (1999).

The contact model described so far, and the resulting forces, are used to update the position and orientation of every particle at each time step. This procedure, i.e. a solution of Newton's equations of motion, is equivalent to that described by Leonardi *et al.* (2014).

HEAP FORMATION AS STUDY-CASE FOR VALIDATION

The implementation of friction and of rolling resistance in the code finds in this work its first application. For this reason, a validation study has been performed, and the results are briefly reported here. Our simulations reproduce the numerical tests performed by Zhou *et al.* (1999, 2002, 2001), who in turn validated their approach with an experimental campaign. The subject of their study is a granular heap created in the process described in Fig. 4. A collection of about 10^4 grains with variable mean diameter D are first collected in a reservoir with

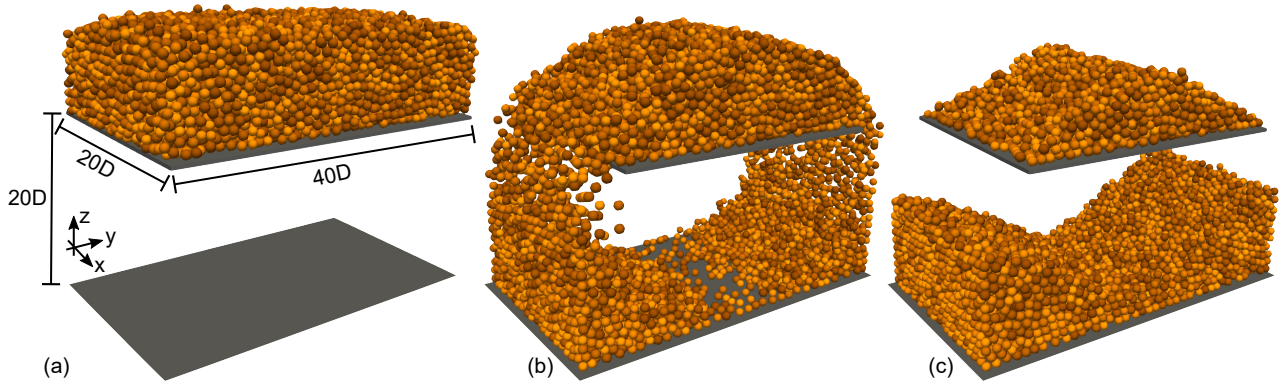

Fig. 4. Geometry for the heap-formation validation test: (a) initial configuration, (b) discharge process, (c) final configuration.

Table 1. Parameters used for the validation test. The parameters coincide with those used by Zhou *et al.* (2002) (note that in this work the definition of μ_r is slightly different).

Parameter values	
Number of particles	10640
Particle diameter D [m]	0.002, 0.005, 0.01
k_n [N/m]	10^6
k_t [N/m]	$\frac{2}{7}k_n$
Restitution coefficient c [-]	0.2
Tangential damping α_t [-]	1.0
Particle-particle friction coefficient μ_s [-]	0.4
Particle-wall friction coefficient $\mu_{s,w}$ [-]	$\frac{3}{2}\mu_{s,p}$
Particle-particle rolling coefficient μ_r [-]	0.05, 0.04, 0.02
Particle-wall rolling coefficient $\mu_{r,w}$ [-]	$2\mu_{r,p}$

dimensions $L_x = 20D$ and $L_y = 40D$ placed over a horizontal plate. Two gates of size $L_g = 5D$ are then opened at the plate sides, causing flow of the largest part of the granular mass onto a surface placed $20D$ below (Zhou *et al.*, 1999). The remaining grains over the plate form a stable structure, whose geometry is a function of the contact parameter, and in particular of the friction coefficient μ_s and the rolling coefficient μ_r.

As in Zhou *et al.* (2002), we use particles of diameter 2, 5, and 10 mm, with density 2500 kg/m^3. All geometrical parameters, such as the box dimensions and the size of the plate, are the same as in the reference numerical tests. A number of differences however exist between the two numerical models. The reference simulations were performed using a Hertzian law for the computation of the normal repulsive force, while our model uses a simpler linear law. While the rolling models are conceptually similar, the reference simulations were performed by Zhou *et al.* (2002) fixing the rolling eccentricity e (see Eq. 1) rather than the rolling coefficient μ_r. As a consequence, particles with different radius need to be modeled with different rolling coefficients in order to obtain exactly the same rolling torque as in the reference numerical experiment. The rolling coefficient, as well as all other relevant parameters used for our numerical simulations, are collected in Table 1. Note that for this set of simulations we use a radius-dependent friction coefficient, only in order to match the dimensional parameters used by Zhou *et al.* (2002). For all simulations presented in the next sections, this choice is dropped in favor of a dimensionless radius-independent coefficient.

The simulations are halted when the residual kinetic energy vanishes. At that point, heaps created by particles of different size exhibit for both models a similar geometry, but a different slope. A summary of the results is presented in Fig. 5. In the figure, the experimental results used by Zhou *et al.* (2002) to validate their model are reported as well. The simulations use much less particles than in the experiments, but the size is the same. The number of simulated particles is however large enough to minimize finite-size effects. The numerical and experimental heaps are comparable, and show a similar dependency of the angle of repose ϕ on the grain size. The angle of repose diminishes when using larger particles, as already observed by Carstensen & Chan (1976).

To objectively evaluate the angle of repose, the heap is divided in direction z into ten segments. The height of each segment is taken as the center of mass of the highest particle belonging there. The points are then linearly interpolated to obtain a measure of the slope. The results of the proposed model, together with those obtained by Zhou *et al.* (2002), and with the experimental dataset of Carstensen & Chan (1976), are quantitatively compared in Fig. 5 (c), showing a common trend.

CONSTITUTIVE MODEL FOR INTERNAL ARCHING

One of the major difficulties, both theoretical and practical, that emerges when dealing with natural granular flows is the determination of the material properties. Natural grains differ in shape, size, and composition, making it hard to characterize the whole mass with few parameters. For this reason, a granular material is usually described using macroscopic characteristics, such as the angle of internal friction ψ obtainable through the standard triaxial test (Cui *et al.*, 2016). For granular flows, where confinement is generally limited and large rates are common, the heap-formation tests is also widely used (e.g. Coetzee & Els, 2009; Grima & Wypych, 2011; Barrios *et al.*, 2013; Utili *et al.*, 2015), allowing to determine the angle of repose of the granular mass ϕ. This latter test is particularly useful when the size of the grains precludes the possibility of using a more precise triaxial shear test.

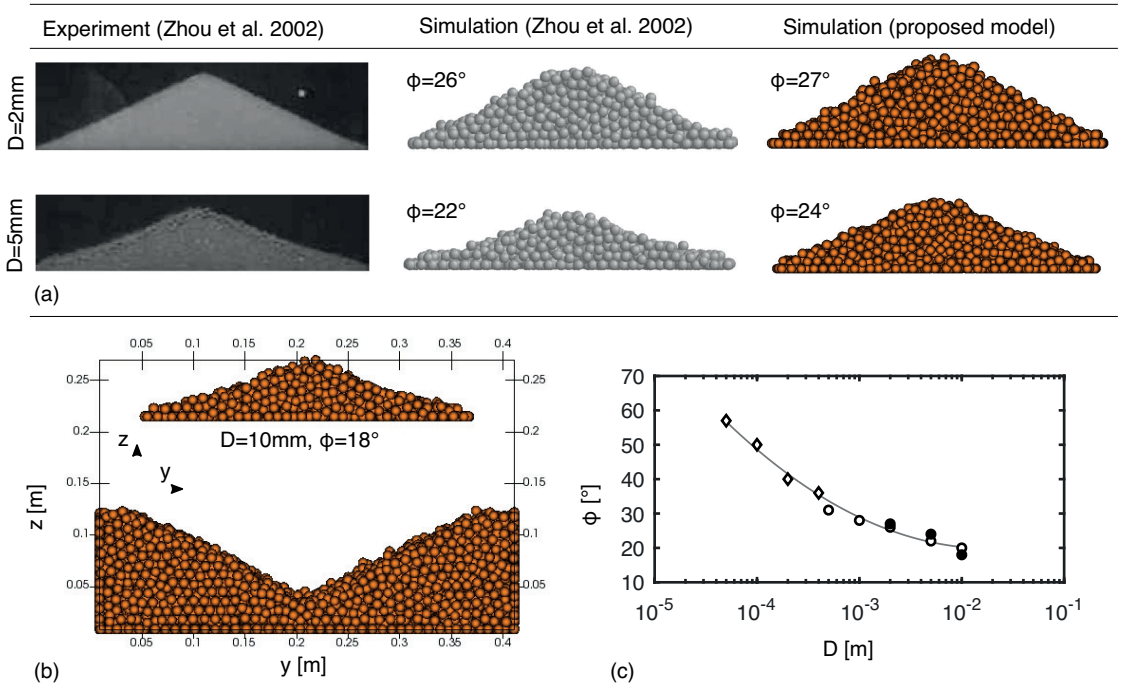

Fig. 5. Comparison of the final experimental and numerical configurations obtained by Zhou *et al.* (2002) and the proposed model. In panel (*a*) the final heaps are compared with the reference experimental and numerical results for $D = 2$ mm and $D = 5$ mm. For the largest particles ($D = 10$ mm) reference pictures are not available, so only our numerical result is shown (*b*). In panel *(c)* the results are quantitatively compared with those presented in the reference. Filled circles are the results obtained with our model, empty circles those obtained numerically by Zhou *et al.* (2002), and diamonds the experimental data of Carstensen & Chan (1976). A logarithmic regression line is plotted as a guide for the eye.

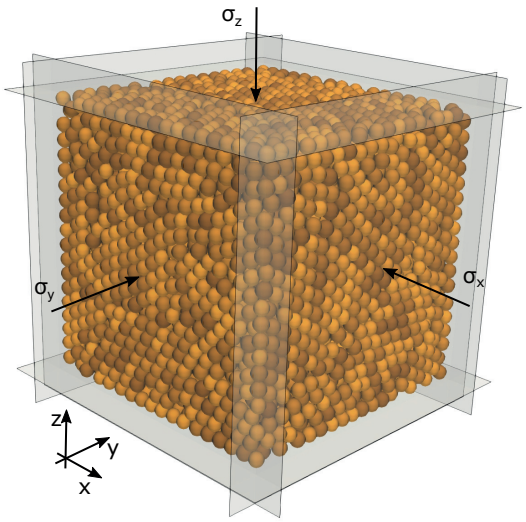

Fig. 6. Setup of the triaxial tests used for identifying the internal friction angle. The gray planes are mobile walls, set to impose a constant pressure σ_i to the granular mass.

For a given particle size, a relationship between the angle of repose ϕ, or the angle of internal friction ψ, and the numerical parameters (μ_s, μ_r) is anyway necessary to characterize the material for the numerical simulations. We therefore proceed to perform a set of triaxial tests to determine the functional relationship for the angle of internal friction, and a series of heap-formation tests to identify an analogous function for the angle of repose.

Table 2. Parameters used for the triaxial and heap-formation tests.

Parameter values	
Number of particles	7640
Volume V [m^3]	4.03
Grain diameter D [mm]	100
Grain density ρ [kg/m^3]	2500
Normal contact stiffness k_n [N/m]	10^6
Tangential contact stiffness k_t [N/m]	$\frac{2}{7}k_n$
Friction coefficient μ_s [-]	0 - 0.2
Rolling coefficient μ_r [-]	0.1 - 0.6

Triaxial tests

Triaxial tests are performed by assembling a sample of ~ 8000 monodisperse particles. In reason of the particle diameter used for the numerical simulations of the flow interaction with a barrier, which will be described in the next section, a diameter of 100 mm has been tested. For this grain size, 209 triaxial tests are performed, varying μ_r from 0.0 to 0.2 with step 0.02 and μ_s from 0.1 to 1.0 with step 0.05, while keeping constant the other parameters, as listed in Table 2. For the friction angle μ_s, the investigated values cover the typical range of values of natural granular materials. The rolling coefficient μ_r spans also relatively large values, which are here used to model the non-sphericity of natural grains.

We follow the procedure described by Zhao *et al.* (2015), and illustrated in Fig. 6. The sample is initially compressed in isotropic conditions by imposing a constant pressure at all walls

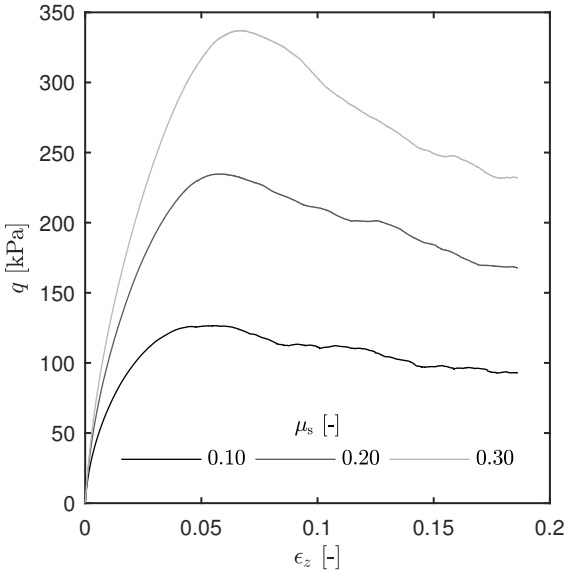

Fig. 7. Stress-strain evolution during three sample triaxial test, with fixed $\mu_r = 0.08$ and variable μ_s.

$\sigma_x = \sigma_y = \sigma_z = 100$ kPa. This initial phase is performed with $\mu_r = 0$ and $\mu_s = 0$ in order to obtain a dense packing. After this, a secondary phase begins, with the sample compressed in direction z at a constant strain rate ($\sim 2 \cdot 10^{-4}$ s^{-1}), i.e. controlling the axial strain ϵ_z, while keeping a constant pressure at the side walls. At each instant, the mean and deviatoric stresses are computed, respectively, as

$$\begin{cases} p = (\sigma_x + \sigma_y + \sigma_z)/3 \\ q = (\sigma_z - \sigma_x). \end{cases} \tag{2}$$

Typical stress/strain recordings are illustrated in Fig. 7. All samples exhibit a peak stress, followed by a decay to a residual value for large strains.

The peak and residual shear strengths can be analyzed to obtain a peak and residual macroscopic internal friction angle, respectively ψ_{peak} and ψ_{res}. Fig. 8 (*a*,*b*) shows the results obtained with the parameters described above. A specific value of the internal friction angle (both peak and residual) can be obtained by multiple combinations of (μ_s, μ_r). It is observed that the rolling resistance has a limited influence on the internal friction angles.

Heap-formation tests

The heap-formation tests are performed using the heap-formation procedure described in the previous section, and the geometrical parameters listed in Table 2. As shown in the previous section, the angle of repose depends on the particle size. It is moreover a function of friction and rolling resistance (Zhou *et al.*, 2001). Such a relationship cannot be inferred directly, because of the strong non-linearity of the problem.

To overcome this, and in analogy to the triaxial tests, a large number of numeral simulations is here performed, each reproducing the heap-formation test described in the previous section for a different set of parameters (μ_s, μ_r). Notably, the presence of both rolling and sliding resistance is a necessary condition for heap formation. When either μ_s or μ_r is zero, a stable heap cannot form on a horizontal plane, and accordingly a granular assembly cannot be halted on an incline, independently of the slope.

The results of the heap-formation simulations are collected in Fig. 8 (*c*). For large values of μ_r (the upper parts of the contours), the results of the angle of repose are very similar to the residual angle obtained with the triaxial tests. On the other hand, a low rolling coefficient always leads to unphysically low angles of repose, independently from the magnitude of the friction coefficient (Utili *et al.*, 2015).

The same figure also shows the results obtained with the formulation proposed by Zhou *et al.* (2002), rewritten as:

$$\phi = 47 \mu_s^{0.27} \mu_{s,w}^{0.22} \mu_r^{0.06} \mu_{r,w}^{0.12} D^{-0.02}, \tag{3}$$

which has however been obtained for particles with $D < 10$ mm. The original formula had a slightly different appearance, because of the original definition of μ_r and $\mu_{r,w}$ in Zhou *et al.* (1999), where both coefficients have the dimension of a length. Moreover, D was originally expressed in millimeters while in Eq. 3 D is expressed in meters. A good agreement between this formulation and our numerical results is found for the lower values of μ_r and μ_s.

An analytical expression of the functional relationship $\phi = f(\mu_s, \mu_r)$ that fits the obtained numerical results should now be defined to be used as constitutive model for the analyses that will follow. The resulting analytical expression is:

$$\phi = \sqrt{\mu_s a(\mu_r)}, \tag{4}$$

with

$$a(\mu_r) = \begin{cases} 23000 \mu_r & \text{for } \mu_r \leq 0.12 \\ 2800 & \text{for } \mu_r > 0.12. \end{cases} \tag{5}$$

Restricting the domain of validity to $\mu_r \leq 0.12$ and $\mu_s \leq 0.7$, the formulation can be simplified to:

$$\phi = 150 \sqrt{\mu_s \mu_r}. \tag{6}$$

It is evident that, as in the triaxial tests, the simplified formulation can lead to the same angle of repose ϕ with multiple combinations of values (μ_s, μ_r). Eq. 6 provides a link between an easily identifiable physical parameters (ϕ) and the internal numerical parameters μ_s and μ_r. This allows to reproduce real granular material with a degree of confidence, as will be performed in the next section.

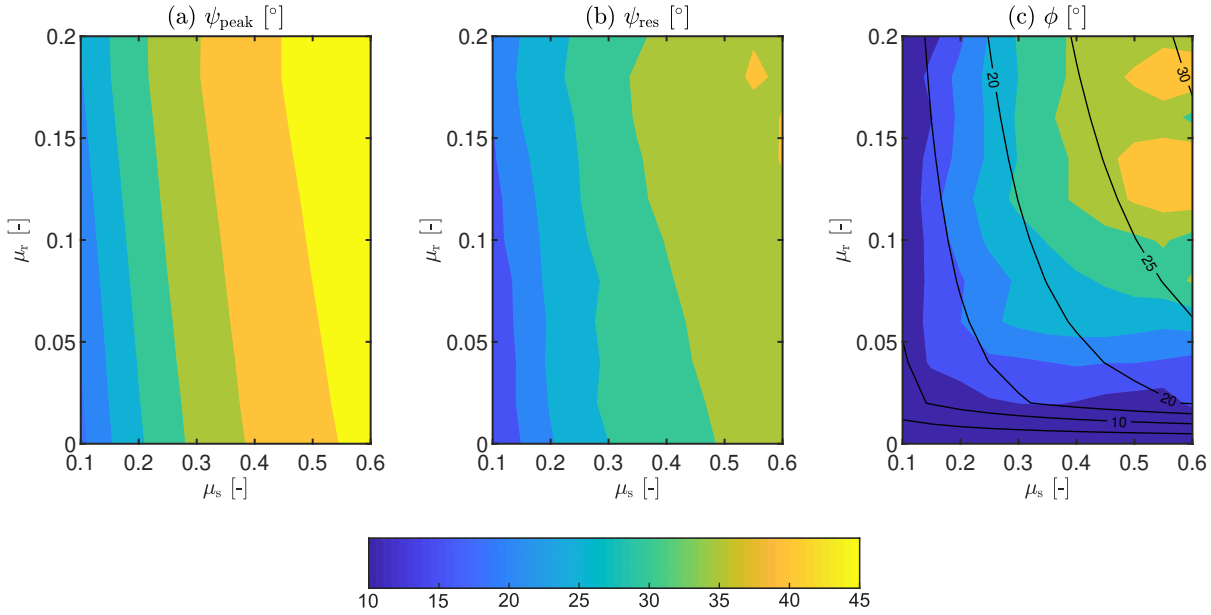

Fig. 8. Filled-contour representation of the functional relationship between the macroscopic resistance parameters of the material obtained with the simulations, and the DEM parameters: friction coefficient μ_s and rolling coefficient μ_r. (*a*) Peak internal friction angle from triaxial tests ψ_{res}. (*b*) Residual internal friction angle from triaxial tests ψ_{peak}. (*c*) Angle of repose from the heap-formation tests ϕ. For comparison, the results obtained with Eq. 3 by Zhou *et al.* (2002), for particles with $D < 10$ mm are plotted in this panel with solid lines.

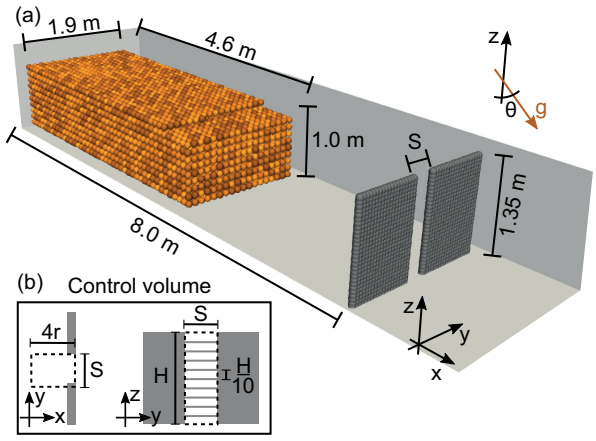

Fig. 9. (a) Geometrical setup used for the slit-dam simulations. The gravity vector, g in the figure, is rotated to obtain the desired inclination. (b) Geometrical description of the control volume used for evaluating the kinetic status of the grains at the outlet.

Table 3. Geometry and characteristic parameters used for the slit-dam simulations.

Parameter	Values
Number of particles	7640
Released volume V [m^3]	4.03
Grain diameter D [mm]	100
Grain density ρ [kg/m^3]	2500
Normal contact stiffness k_n [N/m]	10^6
Tangential contact stiffness k_t [N/m]	$\frac{2}{7}k_n$
Restitution coefficient c [-]	0.8
Friction coefficient μ_s [-]	0.58
Rolling coefficient μ_r [-]	0.068
Particle-wall rolling coefficient $\mu_{r,w}$ [-]	$2\mu_r$

IMPACT OF A GRANULAR FLOW ON A SLIT BARRIER

Simulation setup

As stated in the introduction, a simulation set is here proposed with the goal of reproducing a simplified but realistic setting. The adopted geometry aims at mimicking a slit-check dam such as the one depicted in Fig. 1. The setup consists of an idealized channel with rectangular section. The channel is 20 m long and 1.9 m wide, and can be inclined to obtain the desired slope θ. An orthogonal reference system linked to the local topography is used, with the z axis normal to the channel floor, and the x-axis oriented downslope, as depicted in Fig. 9.

An open barrier extends over the whole width of the domain in the yz plane, and has a vertical outlet in its central part. An assembly of compacted spheres, which can deform and exchange forces if impacted, but whose motion is prevented, is used to model the barrier.

The granular mass is composed of spherical particles with mean diameter $D = 100$ mm. The particles are initially arranged in a cubic pattern, which however breaks rapidly during the first instants of flow. A small degree of dispersion ($\pm 5\%$) is used for the particle radius, in order to limit crystallization (Bi *et al.*, 2005). It remains very hard to avoid a certain degree of crystallization in the bottom layer of the flow, because of the contact with a flat surface.

The granular flow is obtained by collapse of the granular mass, whose front is initially located at distance 3.4 m from the barrier. The collapse is driven by gravity alone (Fig. 9). The release scheme is equivalent to that obtained with a dam-break setup, which is a common choice when simulating the interaction with structures (Gabrieli & Ceccato, 2016). As already mentioned, with the aim of investigating the outlet clogging mechanism, only the coarsest grains are modeled.

Table 4. Flow parameters, measured before impact at the front, here identified as the section located 1 m behind the foremost particle.

Flow parameters before impact					
θ [°]	10	20	30	35	40
θ/ϕ [−]	0.33	0.67	1.00	1.17	1.33
v_f [m/s]	3.62	5.38	7.08	7.83	8.25
h_f [m]	0.24	0.26	0.28	0.36	0.41
Fr [-]	2.31	3.37	4.27	4.17	4.11

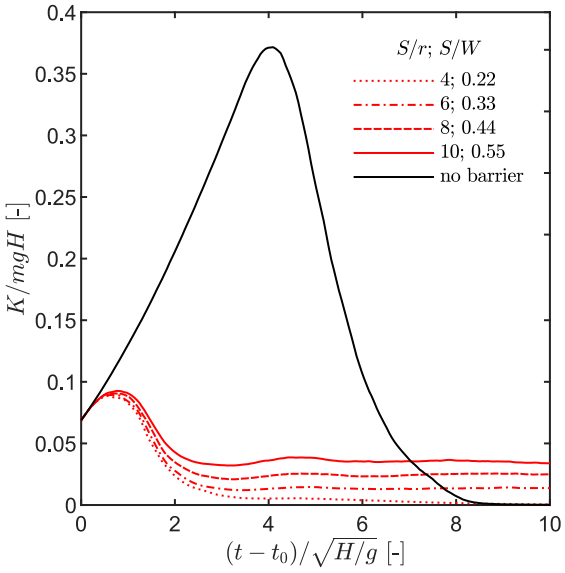

Fig. 10. Kinetic energy of the flow K registered for different barrier configurations.

Overflow is prevented by fixing the height of the channel and of the barrier to $H = 1.35$ m. The width of the channel, being 18 times the grain diameters D, is set in order to limit the influence of the domain lateral walls (Pournin *et al.*, 2007). All domain boundaries are made of rigid walls, with frictional properties.

Debris material is known to form deposit of relatively low angle of repose, down to $\phi = 10^\circ$ or less (Kwan, 2012). This is due to many factors, among which the friction-inhibiting effects of pore fluid pressure. However, we assumed in this work that the slit induces dry conditions to the grains, since the pore fluid can filter. This allows to conservatively represent the intensity of frictional arches. Therefore, a macroscopic angle of repose $\phi = 30^\circ$ is chosen, a typical value for dry coarse grains. The material parameters $\mu_\mathrm{r} = 0.068$, $\mu_\mathrm{s} = 0.58$ are therefore used, in accordance to Eq. 6. The ratio between the slope inclination and the repose angle, θ/ϕ is set by changing the former, with the latter fixed at $\phi = 30^\circ$.

Energy-breaking efficiency

After release, the flow quickly accelerates, but does not reach a steady state before hitting the barrier. Varying the ratio θ/ϕ gives origin to flows with different velocities. An estimation of the front velocity v_f and of the flow height at the front h_f is given in Table 4. These are obtained by measuring the properties 1 m behind the front particle. From these parameters, a Froude number can be defined as $\mathrm{Fr} = v_\mathrm{f}/\sqrt{gh_\mathrm{f}}$. However, this definition is not objective, because the flow is not uniform, and because different methods for measuring v_f and h_f can give substantially different results.

In any case, after impact has occurred, inertia becomes less important. The kinetic energy of the flow, computed as

$$K = \sum_{i=1}^{N} \left(\frac{1}{2} m_i v_i^2 + \frac{1}{2} I_i \omega_i^2 \right), \tag{7}$$

is shown in Fig. 10. The kinetic energy is measured only in the portion of the domain located upstream of the barrier position, regardless of the presence of the barrier. When the flow is undisturbed, i.e. when no barrier is present, K grows much larger than in presence of the barrier. This is true even for relatively large openings.

To quantify the energy dissipation induced by the barrier, we define an energy-breaking efficiency as:

$$E_K = \frac{\int_{t_0}^{t} K_\mathrm{undisturbed} - K_\mathrm{barrier} \mathrm{d}t}{\int_{t_0}^{t} K_\mathrm{undisturbed} \mathrm{d}t}. \tag{8}$$

where t_0 is the instant at which first impact occurs. The measurement window is limited to the first 10 dimensionless time units, see Fig. 10.

It is apparent that the barrier energy-breaking efficiency is always very high. It is also a weak function of the channel inclination. This is true even for relatively large slits ($S/W = 0.6$). The kinetic energy collapses to its final, stable value in about 4 dimensionless time units (Fig 10). From that moment, the flow inertia, and the initial Froude condition, appear to have a negligible effect. The interactions that lead to clogging are therefore governed by an interplay between gravitational forces and friction, which is best represented by the ratio θ/ϕ.

Retention efficiency

For each ratio θ/ϕ, a study of the barrier retention efficiency has been performed by varying the outlet width S (Fig. 9), geometrically normalized by the characteristic radius of the grains r, to identify the critical outlet size that prevents clogging formation. The investigated ratios S/r range from 2 to 10.

In the literature, there is little information about the critical ratio that causes grain stoppage in the outlet for this configuration. A few early experimental works (Ikeya & Uehara, 1980; Mizuyama *et al.*, 1988) suggest a slit size $S/r < 3$, and a recent work by Shima *et al.* (2016) surveyed filter dams, confirming that trapped boulders had a size corresponding to $S/r < 3 - 4$. There is however a rich literature that studies clogging in silos (Pournin *et al.*, 2007; Hidalgo *et al.*, 2013).

A key difference between a silos and a slit barrier is the different type of symmetry. The radial symmetry of silos is

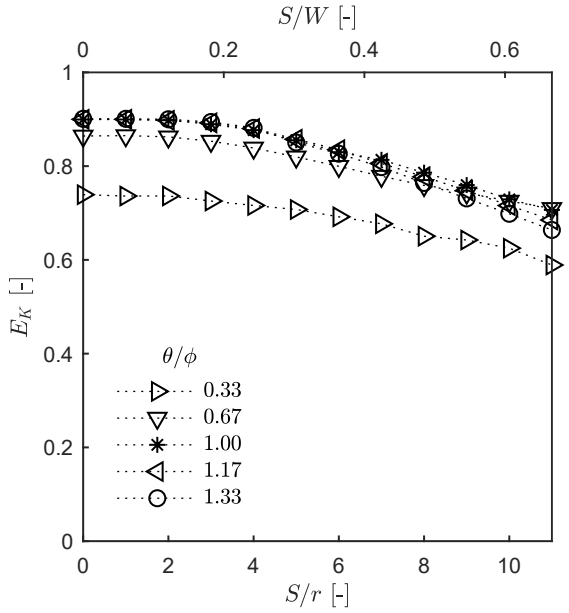

Fig. 11. Energy-breaking efficiency of the barrier E_K as a function of the outlet size S/r, of the transverse blockage S/W, and of the ratio between slope incline and angle of repose θ/ϕ.

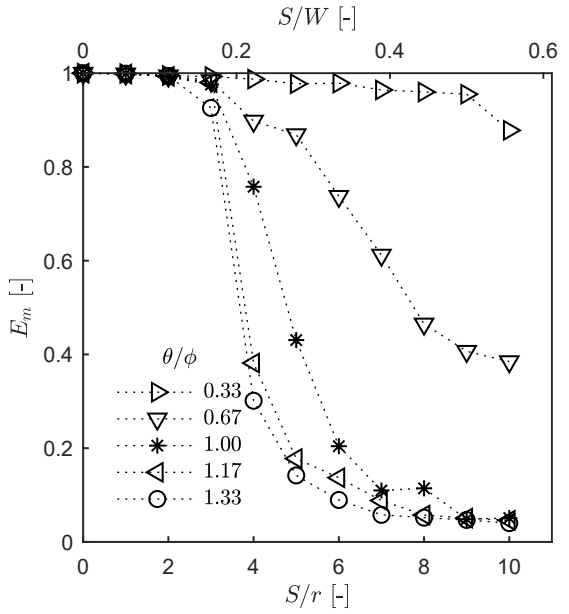

Fig. 12. Retention efficiency of the barrier E_m as a function of the outlet size S/r, of the transverse blockage S/W, and of the ratio between slope incline and angle of repose θ/ϕ.

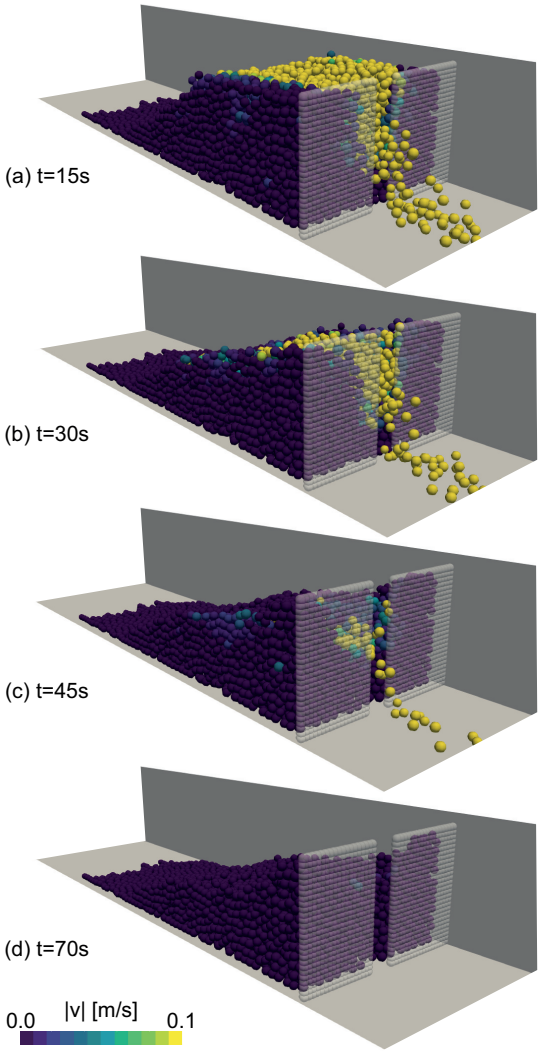

Fig. 13. Example of clogging of a barrier outlet with $S/r = 5$, $\theta/\phi = 1.17$. The presented time sequence evidences the progressive clogging of the barrier outlet and stoppage of the flowing mass.

here reduced to a simple planar symmetry. Additionally, gravity is orthogonal to the outlet in silos, while here it is inclined. Therefore, the intensity of the forces that sustain the arches clogging the outlet is stronger at the bottom of the deposit than at the top. It remains however possible to transfer core concepts. A typical lower value of the ratio S/r that prevents clogging in silos falls in the range $3 < S/r \leq 6$ (Magalhães *et al.*, 2015; Arévalo & Zuriguel, 2016). However, the exact value depends on the specific geometry, and on the type of grains. Typically, 2D silos clog more easily than their 3D counterpart (Janda *et al.*, 2008), since they require the formation of a simple arch rather than more complex dome-like structure. Analogously, the slit barrier promotes the formation of a 3D stable structure, but a thin flow composed of a single layer of particles can anyway form an arch similar to those observed in 2D silos.

In this work, the retention efficiency is defined as

$$E_m = \frac{m_{\text{stop}} - m_{\text{base}}}{m_{\text{tot}} - m_{\text{base}}}, \tag{9}$$

and expresses the ratio between the mass halted by the barrier at the end of the simulation m_{stop} and the total released mass m_{tot}. Both are net of the mass that stops because of basal friction alone m_{base}, which is estimated by running simulations without the barrier. Note that m_{base} is relevant only for gentle slopes. A fully closed barrier ($S = 0$) or very large grains with respect to the outlet size ($S/r \to 0$) always determine unitary retention efficiency.

The simulation results are presented in Fig. 12. A key difference in mechanism is observed between steep slopes ($\theta/\phi > 1$) and gentle slopes ($\theta/\phi < 1$). On gentle slopes, the mass halts regardless of the presence of the barrier, as the repose angle is larger than the imposed incline. Note that

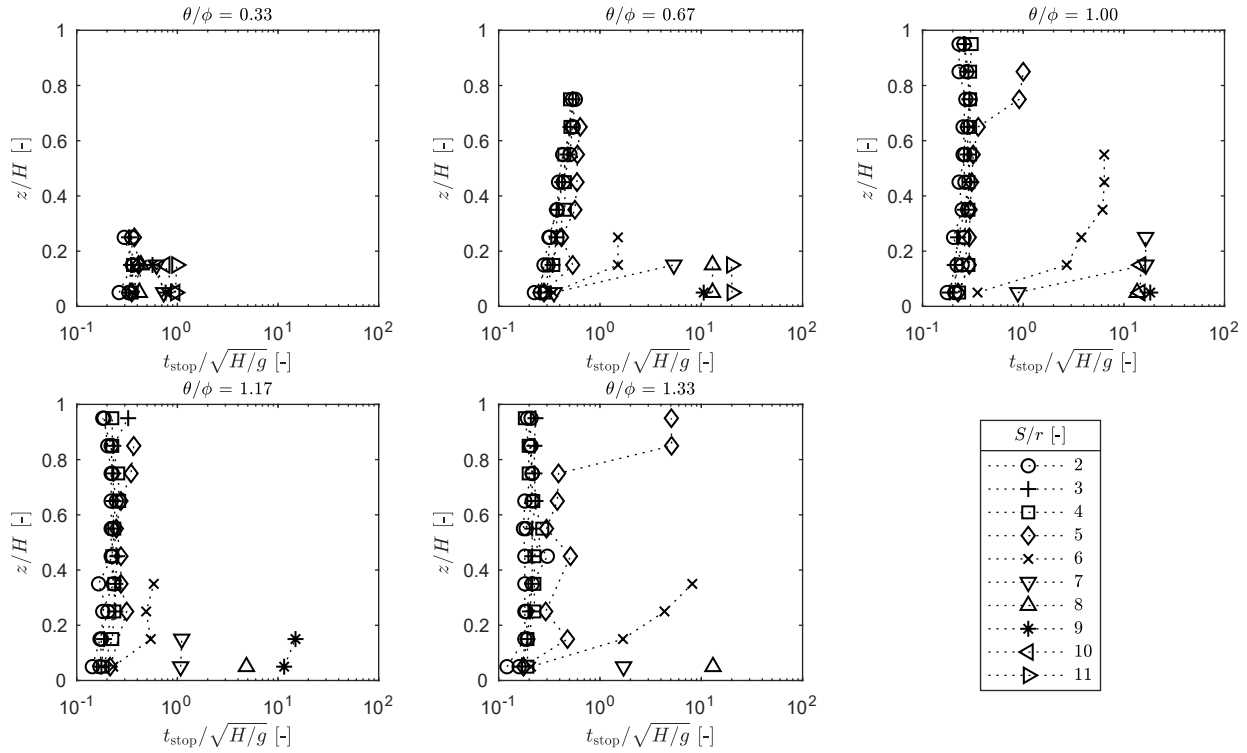

Fig. 14. Clogging time (t_{stop}) at different heights along the barrier as a function of θ/ϕ and S/r.

even in this condition an initial flow originates by the initial clump of the granular mass. In all simulated cases, this initial clump is sufficient to let a portion of the mass reach the barrier. The stopping of particles is then always attributable to a combination of the presence of the barrier and of basal friction, with the latter becoming dominant on gentle slopes. On steep slopes ($\theta/\phi > 1$) the curve follows an S shape typical of smooth phase transitions. For $S/r \to \infty$, zero retention efficiency is expected as basal friction is not high enough to halt the flow, and stable structures cannot clog the outlet. However, a small amount of material always remains behind the barrier wings, therefore zero retention efficiency is never achieved in practice.

THE CLOGGING MECHANISMS

Transition from flow condition to stable structures

The results of the previous section only concern the analysis of the system final configuration. However, a richness of behaviors can be observed when investigating the paths that lead to the final configuration.

In some of the analyzed cases, grain stoppage is almost instantaneous, with the immediate formation of a stable 3D granular structure that covers the full height of the barrier. In some others, a stable configuration is finally reached, but this takes a long time, such as in the example provided in Fig. 13. For the latter, although a rapid decrease of the kinetic energy of the flow is immediately observed, a stable granular structure forms much later, but does not completely cover the outlet. A progressive growth of the clogging height is then reached through the alternation of locking and unlocking of the outlet. Consecutive remobilizations of already stopped grains cause small overflows of material, which in turn promote further rearrangements of the particles and a delay in time before reaching the final configuration.

A progressive clogging of the dam outlet can be speculated as being a favorable process. It provides a modulation of the kinetic energy, while at the same time limiting the amount of halted material, and therefore guaranteeing a longer lasting effectiveness of the barrier during an event.

To identify the conditions under which progressive clogging occurs, the kinetic energy of the mass is tracked as a function of time and position. To this aim, a control volume extending upstream from the barrier is taken as reference. This volume consists of a cuboid having the same width and height of the outlet and a length equal to $4r$ in the x direction. This is divided into ten equal-thickness layers. Each layer is identified by the midpoint of its thickness in the z direction and contains a number N of particles (Fig. 9 b). The kinetic energy of the particles in a layer is evaluated using Eq. 7. If particles are present, but their kinetic energy is negligible (we use as threshold $K < 10^{-5}$J), that layer is considered clogged. The time interval between the first impact of the released particles on the barrier and the particle clogging in each z-layer is called clogging time, and indicated as $t_{stop}(z)$.

The diagrams showing t_{stop} for different θ/ϕ and S/r ratios are illustrated in Fig. 14. Here, t_{stop}, scaled by $\sqrt{H/g}$, is represented as a function of z/H, with H the total height of the barrier. For gentle slopes (especially for $\theta/\phi = 0.33$), clogging occurs rapidly (usually within the first 50 s) but on average concerns a small number of layers. This can be justified

by the large number of particles that in these configurations stop before reaching the barrier. In these cases, the barrier only anticipates particle stoppage, which would anyway occur because of the low channel slope.

For steep slopes, four possible patterns can be identified Fig. 15). When the outlet is very narrow ($S/r < 4$), clogging occurs rapidly, and concerns the full outlet height. Vice versa, if the outlet is very wide ($S/r > 9$) clogging does not occur at all. These two configurations are respectively called "Rapid" and "Ineffective", and are indicated in Fig. 15 as *R* and *I*. The results agree with those obtained by Arévalo & Zuriguel (2016) on a 2D inclined silos, where the range for ineffective clogging starts when $S/r > 10$.

Usually, the critical S/r ratio that promotes clogging is identified in between the two configurations described above. In this respect, the simulations evidence that there is an intermediate range of S/r values for which two further configurations are possible. The first involves clogging of a significant height of the outlet, but with some delay in time (especially for the upper layers). This implies that the flows last for a relatively long time, but stoppage is eventually achieved, with the grains forming a stable, three-dimensional structure. This clogging mechanism is indicated as "Progressive", *P* in Fig. 15. Finally, a scenario is observed in which clogging occurs with delay in time, the barrier retention efficiency is very low, and yet a stable structure forms nevertheless. Usually, in this case the particles at direct contact with the barrier form a single-layer 2D arch. This is indicated as "Bidimensional", *B* in Fig. 15. Note that upstream of the arch, the deposit is not necessarily composed of a single layer.

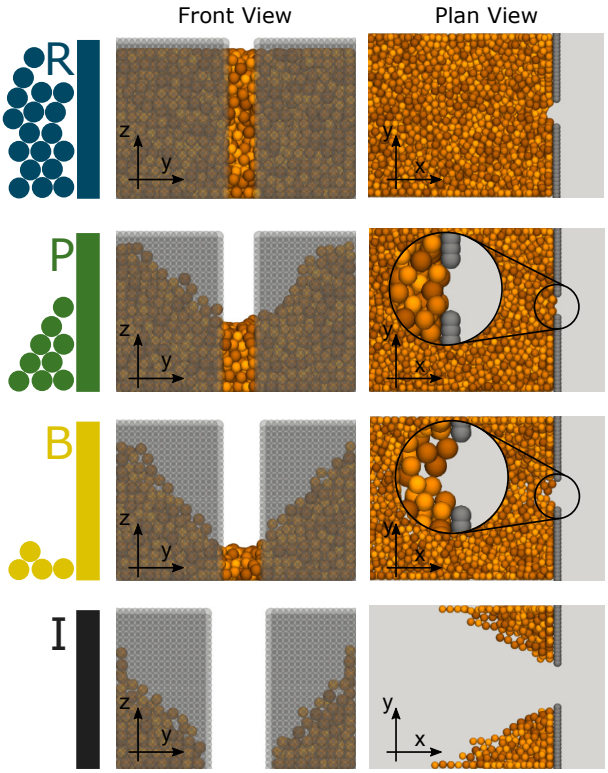

Fig. 15. Possible types of clogging mechanisms. The examples are from simulations with $\theta/\phi = 1.17$ R: rapid ($S/r = 4$), P: Progressive ($S/r = 5$), B: Bidimensional ($S/r = 6$), I: Ineffective ($S/r = 10$). The sketches on the left column idealize the type of clogging associated with each mechanism.

State diagram

The final configuration for all performed simulations, arranged in a state diagram with θ/ϕ and S/r as axis, is indicated in Fig. 16. Markers of different color correspond to the four described mechanisms. From a perspective of barrier effectiveness, progressive clogging is desirable, as the material is released slowly, and a longer timeframe of barrier effectiveness is guaranteed. Bidimensional clogging is however more commonly encountered in the simulations, covering a larger portion of the state diagram studied with Fig. 16. Even when the clogging mechanism on the outlet is bidimensional, the material behind the barrier can be large, as shown in Fig. 15. It remains to be further investigated whether the dominance of the bidimensional clogging pattern is an artifice introduced by the simplified geometry, or a behavior that is more common also in reality.

Bidimensional clogging dominates the portion of the diagram related to gentle slopes. As already discussed, in this case a single bidimensional arch does not hold the whole mass into place, but rather anticipates a stoppage that would occur anyway due to the large friction coefficients. It should be stressed that usually retention structures are located where slopes are gentle ($\theta < \phi$). However, in natural granular flows the frictional resistance of the material is often reduced because of additional internal mechanisms that enhance mobility, such as excess pore pressure (Kaitna *et al.*, 2016). For this reason, the part of the diagram related to steep slopes is still significant.

The final recommendation depends strongly on the design perspective. If a complete stoppage of boulders larger than a given size r^* is necessary, a small S/r^* should be chosen, guaranteeing clogging with rapid characteristics. In alternative, the barrier can be designed to perform energy-breaking and filtering functions while at the same time limiting the amount of material that needs to be removed after each event. This would guarantee a long-term effectiveness of the barrier itself. In this case, it results that the range $6 < S/r^* < 7$ covers the area where the best behavior, i.e. where progressive mechanism dominates. Also in case of a phenomenon with multiple surges, which is typical of debris flows, progressive clogging could to some extent prevent a quick filling of the barrier, allowing the barrier itself to remain functional for multiple surges.

CONCLUSIONS AND FURTHER DEVELOPMENTS

The debris flows impact on mitigation structures is still a problem not fully understood, especially because of the complexity of debris material. Generalizing the results of experimental and numerical studies remains difficult. It is nevertheless important to address this complexity, and update the existing guidelines and prescriptions in order to define a

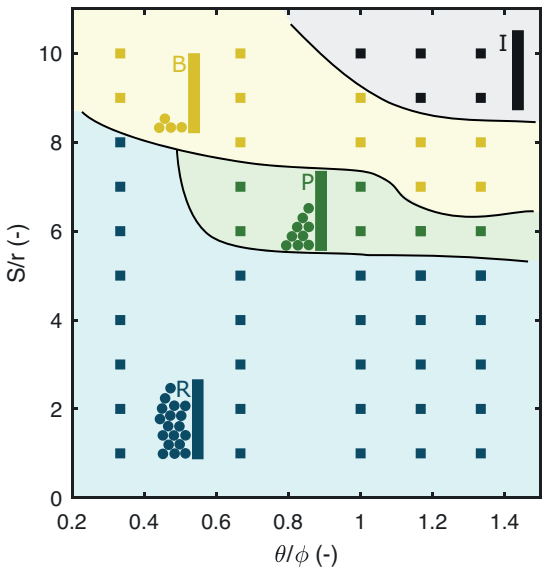

Fig. 16. Diagram of the clogging mechanisms observed at the end of the carried-out simulations. Refer to Fig. 15 for the definition of the mechanisms and the legend for the symbols. Each marker corresponds to a simulation for a different set of values (θ/ϕ, S/r).

more rational procedure for the design of these structures. In the perspective of hazard mitigation, it is desirable to build effective and efficient structures that possibly require minimum maintenance. At the same time, the amount of construction material should be optimized, as these structures are often built inside natural environments.

Numerical simulation can potentially give a contribution. For this reason, a model has been proposed, able to simulate the interaction between a dry granular flow and a slit-check dam. The model has been validated by comparing with previous experimental and numerical results on heap formation. While still relying on severe simplifications, the model can address the specific problem of clogging of the barrier outlet with unprecedented precision.

The internal friction angle and the angle of repose have been chosen as the macroscopic parameters for the characterization of the granular material. Both have been correlated with the numerical parameters of the contact model, yielding constitutive relations. As an improvement with respect to previous studies (Teufelsbauer *et al.*, 2009; Law *et al.*, 2016), this allows to link the model parameters to observable properties of the coarse grains.

Concerning the mechanism of interaction between granular flow and slit-check dam, a two-dimensional parametric space has been studied. We explored the effects of the ratio between channel slope and angle of repose of the grains θ/ϕ, and of the ratio between slit opening width and grain size, S/r. Both have a strong effect on the type of behavior observed. In particular, four recurring clogging mechanisms have been identified. An obvious result is that for large S/r, most of the material flows beyond the barrier, while a very small S/r determines a quick clog of the outlet. In the intermediate range, clogging has been shown to occur progressively. Overall, a ratio between $S/r = 6$ and $S/r = 8$ guarantees the best conditions, with an intermediate retention function obtained without abrupt clogging of the outlet. At the same time, the energy-breaking function is guaranteed.

It remains however to be further investigated whether the obtained results, and in particular the described state diagram, are resilient to changes in the setup geometry or in the material. The number of simplifications need to be relaxed before generalizing the results for application in the field. In particular, triggering the flow through collapse of a granular mass, albeit being a standard practice for this type of studies, is unrealistic. A natural flow comes with much larger volumes of debris. Ideally, the mass should enter the domain through an inlet. This poses however severe challenges to the numerical model. This additional complexity will be addressed in future studies, where the results of a full-size simulation will be used to setup an inlet condition. An additional issue is given by the fact that most natural phenomena, e.g. debris flow, come with grains of different size and with an additional fluid phase (Cui *et al.*, 2017a,b). The code we used for this work can possibly simulate fluid-grain mixtures (Leonardi *et al.*, 2013, 2015). However, the simulation of multiphase flows would further complicate the analysis of the results, and is therefore postponed to a future work.

ACKNOWLEDGEMENTS

Computational resources were provided by HPC@POLITO, a project of Academic Computing within the Department of Control and Computer Engineering at Politecnico di Torino (http://www.hpc.polito.it).

REFERENCES

Albaba, A., Lambert, S., Nicot, F., Chareyre, B., Etgr, U. R. & Hères, S.-m. (2015). Modeling the Impact of Granular Flow against an Obstacle. In *Recent Advances in Modeling Landslides and Debris Flows* (Wu, W., ed.), Springer Series in Geomechanics and Geoengineering, Springer International Publishing Switzerland, pp. 95–105, doi:10.1007/978-3-319-11053-0.

Arévalo, R. & Zuriguel, I. (2016). Clogging of granular materials in silos: effect of gravity and outlet size. *Soft Matter* **12**, No. 1, 123–130, doi:10.1039/C5SM01599E.

Armanini, A., Dellagiacoma, F. & Ferrari, L. (1991). From the check dam to the development of functional check dams. In *Fluvial Hydraulics of Mountain Regions* (Armanini, A. & Di Silvio, G., eds.), 1, Springer Berlin Heidelberg, pp. 331–344, doi:10.1007/BFb0011200.

Barrios, G. K., de Carvalho, R. M., Kwade, A. & Tavares, L. M. (2013). Contact parameter estimation for DEM simulation of iron ore pellet handling. *Powder Technology* **248**, 84–93, doi:10.1016/j.powtec.2013.01.063.

Bi, W., Delannay, R., Richard, P., Taberlet, N. & Valance, A. (2005). Two- and three-dimensional confined granular chute flows:

Experimental and numerical results. *Journal of Physics Condensed Matter* **17**, No. 24, 2457–2480, doi:10.1088/0953-8984/17/24/006.

Calvetti, F., di Prisco, C. G. & Vairaktaris, E. (2015). Impact of dry granular masses on rigid barriers. *IOP Conference Series: Earth and Environmental Science* **26**, No. 1, 012036, doi:10.1007/s11440-016-0434-z.

Calvetti, F., di Prisco, C. G. & Vairaktaris, E. (2017). DEM assessment of impact forces of dry granular masses on rigid barriers. *Acta Geotechnica* **12**, No. 1, 129–144, doi:10.1007/s11440-016-0434-z.

Canelli, L., Ferrero, A. M., Migliazza, M. & Segalini, A. (2012). Debris flow risk mitigation by the means of rigid and flexible barriers experimental tests and impact analysis. *Natural Hazards and Earth System Science* **12**, No. 5, 1693–1699, doi:10.5194/nhess-12-1693-2012.

Carstensen, J. T. & Chan, P. C. (1976). Relation between particle size and repose angles of powders. *Powder Technology* **15**, No. 1, 129–131, doi:10.1016/0032-5910(76)80037-X.

Choi, C. E., Goodwin, G. R., Ng, C. W. W., Cheung, D. K. H., Kwan, J. S. H. & Pun, W. K. (2016). Coarse granular flow interaction with slit structures. *Géotechnique Letters* **6**, No. 4, 267–274, doi:10.1680/jgele.16.00103.

Coetzee, C. J. & Els, D. N. J. (2009). Calibration of granular material parameters for DEM modelling and numerical verification by blade-granular material interaction. *Journal of Terramechanics* **46**, No. 1, 15–26, doi:10.1016/j.jterra.2008.12.004.

Cui, Y., Chan, D. & Nouri, A. (2017a). Coupling of solid deformation and pore pressure for undrained deformationa discrete element method approach. *International Journal for Numerical and Analytical Methods in Geomechanics* **41**, No. 18, 1943–1961, doi:10.1002/nag.2708.

Cui, Y., Chan, D. & Nouri, A. (2017b). Discontinuum Modeling of Solid Deformation Pore-Water Diffusion Coupling. *International Journal of Geomechanics ASCE* **17**, No. 8, 04017033, doi:10.1061/(ASCE)GM.1943-5622.0000903.

Cui, Y., Nouri, A., Chan, D. & Rahmati, E. (2016). A new approach to DEM simulation of sand production. *Journal of Petroleum Science and Engineering* **147**, 56–67, doi:10.1016/j.petrol.2016.05.007.

Gabrieli, F. & Ceccato, F. (2016). Impact of Dry Granular Flows on a Rigid Wall: Discrete and Continuum Approach. *Procedia Engineering* **158**, 152–157, doi:10.1016/j.proeng.2016.08.421.

Girolami, L., Hergault, V., Vinay, G. & Wachs, A. (2012). A three-dimensional discrete-grain model for the simulation of dam-break rectangular collapses: Comparison between numerical results and experiments. *Granular Matter* **14**, No. 3, 381–392, doi:10.1007/s10035-012-0342-3.

Grima, A. P. & Wypych, P. W. (2011). Development and validation of calibration methods for discrete element modelling. *Granular Matter* **13**, No. 2, 127–132, doi:10.1007/s10035-010-0197-4.

Hidalgo, R. C., Lozano, C., Zuriguel, I. & Garcimart\'in, a. (2013). Force analysis of clogging arches in a silo. *Granular Matter* **15**, No. 6, 841–848, doi:10.1007/s10035-013-0451-7.

Hungr, O., Evans, S. G., Bovis, M. J. & Hutchinson, J. N. (2001). A Review of the Classification of Landslides of the Flow Type. *Environmental and Engineering Geoscience* **7**, No. 3, 221–238.

Hungr, O. & Jakob, M. (2005). *Debris-flow Hazards and Related Phenomena*. Springer-Verlag Berlin Heidelberg, doi:10.1007/b138657.

Ikeya, H. & Uehara, S. (1980). Experimental Study about the Sediment Control of Slit Sabo Dams. *Journal of the Japan Society of Erosion Control Engineering* **32**, No. 3, 37–44.

Iverson, R. M. (2015). Scaling and design of landslide and debris-flow experiments. *Geomorphology* **244**, 9–20, doi:10.1016/j.geomorph.2015.02.033.

Janda, A., Zuriguel, I., Garcimartín, A., Pugnaloni, L. A. & Maza, D. (2008). Jamming and critical outlet size in the discharge of a two-dimensional silo. *Epl* **84**, No. 4, doi:10.1209/0295-5075/84/44002.

Kaitna, R., Palucis, M. C., Yohannes, B., Hill, K. M. & Dietrich, W. E. (2016). Effects of coarse grain size distribution and fine particle content on pore fluid pressure and shear behavior in experimental debris flows. *Journal of Geophysical Research: Earth Surface* **121**, No. 2, 415–441, doi:10.1002/2015JF003725.

Koo, R. C., Kwan, J. S., Ng, C. W., Lam, C., Choi, C. E., Song, D. & Pun, W. K. (2017). Velocity attenuation of debris flows and a new momentum-based load model for rigid barriers. *Landslides* **14**, 617–629, doi:10.1007/s10346-016-0715-5.

Kwan, J. (2012). Supplementary Technical Guidance on Design of Rigid Debris-resisting Barriers. *Technical Report 270*, Geotechnical Engineering Office, Hong Kong.

Law, R. P. H., Choi, C. E. & Ng, C. W. W. (2016). Discrete-element investigation of influence of granular debris flow baffles on rigid barrier impact. *Canadian Geotechnical Journal* **53**, No. 1, 179–185, doi:10.1139/cgj-2014-0394.

Leonardi, A., Cabrera, M., Wittel, F. K., Kaitna, R., Mendoza, M., Wu, W. & Herrmann, H. J. (2015). Granular-front formation in free-surface flow of concentrated suspensions. *Physical Review E - Statistical, Nonlinear, and Soft Matter Physics* **92**, No. 5, 052204, doi:10.1103/PhysRevE.92.052204.

Leonardi, A., Pokrajac, D., Roman, F., Zanello, F. & Armenio, V. (2018). Surface and subsurface contributions to the build-up of forces on bed particles. *Journal of Fluid Mechanics* **851**, 558–572, doi:10.1017/jfm.2018.522.

Leonardi, A., Wittel, F. K., Mendoza, M. & Herrmann, H. (2014). Coupled DEM-LBM method for the free-surface simulation of heterogeneous suspensions. *Computational Particle Mechanics* **1**, No. 1, 3–13, doi:10.1007/s40571-014-0001-z.

Leonardi, A., Wittel, F. K., Mendoza, M. & Herrmann, H. J. (2013). Multiphase Debris Flow Simulations with the Discrete Element Method Coupled with a Lattice-Boltzmann Fluid. In *III International Conference on Particle-based Methods Fundamentals and Applications* (Bischoff, M., Ramm, E., Oñate, M., Owen, R. & Wriggers, P., eds.), Stuttgart, pp. 276–287.

Leonardi, A., Wittel, F. K., Mendoza, M., Vetter, R. & Herrmann, H. J. (2016). Particle-Fluid-Structure Interaction for Debris Flow Impact on Flexible Barriers. *Computer-Aided Civil and Infrastructure Engineering* **31**, No. 5, 323–333, doi:10.1111/mice.12165.

Luding, S. (2008). Introduction to discrete element methods: Basic of contact force models and how to perform the micro-macro transition to continuum theory. *European Journal of Environmental and Civil ...* **12**, 785–826, doi:10.1080/19648189.2008.9693050.

Magalhães, F. G. R., Atman, a. P. F., Moreira, J. G. & Herrmann, H. J. (2015). Analysis of the velocity field of granular hopper flow. *Granular Matter* **18**, No. 2, 1–11, doi:10.1007/s10035-016-0636-y.

Mizuyama, T., Suzuki, H., Oikawa, Y. & Morita, A. (1988). Experimental Study on Permeable Sabo Dam. *Journal of the Japan Society of Erosion Control Engineering* **41**, No. 2, 21–25, doi:https://doi.org/10.11475/sabo1973.41.2{_}21.

Ng, C. W., Choi, C. E., Goodwin, G. R. & Cheung, W. W. (2017). Interaction between dry granular flow and deflectors. *Landslides* **14**, No. 4, 1375–1387, doi:10.1007/s10346-016-0794-3.

Piton, G. & Recking, A. (2016). Design of Sediment Traps with Open Check Dams. I: Hydraulic and Deposition Processes. *Journal of Hydraulic Engineering* **142**, No. 2, 04015045, doi:10.1061/(ASCE)HY.1943-7900.0001048.

Pournin, L., Ramaioli, M., Folly, P. & Liebling, T. M. (2007). About the influence of friction and polydispersity on the jamming behavior of bead assemblies. *European Physical Journal E* **23**, No. 2, 229–235, doi:10.1140/epje/i2007-10176-5.

Roux, J. N. & Combe, G. (2002). Quasistatic rheology and the origins of strain. *Comptes Rendus Physique* **3**, No. 2, 131–140, doi:10.1016/S1631-0705(02)01306-3.

Schwindt, S., Franca, M. J., De Cesare, G. & Schleiss, A. J. (2017). Analysis of mechanical-hydraulic bedload deposition control measures. *Geomorphology* **295**, No. March, 467–479, doi:10.1016/j.geomorph.2017.07.020.

Shima, J., Moriyama, H., Kokuryo, H., Ishikawa, N. & MIZUYAMA, T. (2016). Prevention and Mitigation of Debris Flow Hazards by Using Steel Open-Type Sabo Dams. *International Journal of Erosion Control Engineering* **9**, No. 3, 135–144.

Teufelsbauer, H., Wang, Y., Chiou, M. C. & Wu, W. (2009). Flow-obstacle interaction in rapid granular avalanches: DEM simulation and comparison with experiment. *Granular Matter* **11**, No. 4, 209–220, doi:10.1007/s10035-009-0142-6.

Utili, S., Zhao, T. & Houlsby, G. T. (2015). 3D DEM investigation of granular column collapse: Evaluation of debris motion and its destructive power. *Engineering Geology* **186**, 3–16, doi:10.1016/j.enggeo.2014.08.018.

Zhao, T., Dai, F., Xu, N. W., Liu, Y. & Xu, Y. (2015). A composite particle model for non-spherical particles in DEM simulations. *Granular Matter* **17**, No. 6, 763–774, doi:10.1007/s10035-015-0596-7.

Zhou, Y. C., Wright, B., Yang, R., Xu, B. & Yu, A. (1999). Rolling friction in the dynamic simulation of sandpile formation. *Physica A: Statistical Mechanics and its Applications* **269**, 536553.

Zhou, Y. C., Xu, B. H., Yu, A. B. & Zulli, P. (2001). Numerical investigation of the angle of repose of monosized spheres. *Physical Review E - Statistical Physics, Plasmas, Fluids, and Related Interdisciplinary Topics* **64**, No. 2, 8, doi:10.1103/PhysRevE.64.021301.

Zhou, Y. C., Xu, B. H., Yu, A. B. & Zulli, P. (2002). An experimental and numerical study of the angle of repose of coarse spheres. *Powder Technology* **125**, No. 1, 45–54, doi:10.1016/S0032-5910(01)00520-4.